



BASIC SCIENCE ARTICLE

Cardiovascular fetal-to-neonatal transition: an in silico model

Anneloes G. Munneke¹, Joost Lumens¹ and Tammo Delhaas¹

BACKGROUND: Previous models describing the fetal-to-neonatal transition often lack oxygen saturation levels, homeostatic control mechanisms, phasic hemodynamic signals, or describe the heart with a time-varying elastance model.

METHODS: We incorporated these elements in the adapted CircAdapt model with the one-fiber model for myocardial contraction, to simulate the hemodynamics of the healthy term human fetal circulation and its transition during the first 24 h after birth. The fetal-to-neonatal model was controlled by a time- and event-based script of changes occurring at birth, such as lung aeration and umbilical cord clamping. Model parameters were based on and validated with human and animal data.

RESULTS: The fetal circulation showed low pulmonary blood flow, right ventricular dominance, and inverted mitral and tricuspid flow velocity patterns, as well as high mean ductus venosus flow velocity. The neonatal circulation showed oxygen saturation levels to gradually increase to 98% in the first 15 min after birth as well as temporary left ventricular volume overload.

CONCLUSIONS: Hemodynamics of the term fetus and 24-h-old neonate, as well as the events occurring directly after birth and the transition during the first 24 h after birth, were realistically represented, allowing the model to be used for educational purposes and future research.

Pediatric Research (2022) 91:116–128; <https://doi.org/10.1038/s41390-021-01401-0>

IMPACT:

- With the addition of oxygen saturation levels, homeostatic pressure-flow control mechanisms, and the one-fiber model for myocardial contraction, a new closed-loop cardiovascular model was constructed to give more insight into the healthy term human fetal circulation and its cardiovascular transition during the first 24 h after birth.
- Extensive validation confirmed that the hemodynamics of the term fetus and the fetal-to-neonatal transition were realistically represented with the model.
- This well-validated and versatile model can serve as an education as well as a research platform for in silico investigation of fetal-to-neonatal hemodynamic changes under a wide range of physiological and pathophysiological conditions.

INTRODUCTION

Most of our knowledge of the fetal circulation as well as the fetal-to-neonatal transition at birth is based on animal studies. The relative inaccessibility of the fetus and the extremely high invasiveness of certain measurements are responsible for the lack of human data. Although the human fetal circulation has been studied extensively by Doppler ultrasound imaging, with emphasis on Doppler flow velocity waveforms and blood flow estimates,^{1–3} most of the information regarding blood pressures and oxygen saturation levels of the fetal circulation, as well as data regarding the immediate events occurring at birth, have been derived from sheep.^{4–6}

Multiple mathematical models have been proposed as a tool to study the fetal circulation and the cardiovascular fetal-to-neonatal transition. Sá-Couto et al.⁷ were the first to shed light on the fetal-to-neonatal transition by means of a lumped parameter model of the cardiovascular system, although this model lacked the process of gas exchange and homeostatic control mechanisms. Yigit et al.⁸ included a gas exchange in their model to investigate and compare delayed and immediate cord clamping scenarios, yet used an adaptation time of 10 min for all transitional vessels.

Similar to the fetal-to-neonatal transition models, the lumped parameter models of the fetal circulation^{9–16} rarely include oxygen saturation levels and homeostatic control mechanisms. Furthermore, both models either described hemodynamics only in terms of mean values or relied on the time-varying elastance model of myocardial contraction, thereby neglecting the phenomena underlying contraction.

Given the issues mentioned above, the formulation of a physically correct and detailed model of the fetal circulation and its cardiovascular fetal-to-neonatal transition for the first 24 h after birth, able to describe as many clinically relevant phasic hemodynamic waveforms, appears crucial to a better understanding of the functioning of the fetal and early neonatal cardiovascular system and its responses to stress and disease. The aim of this study was, therefore, to adapt the well-validated and versatile CircAdapt multi-scale model of the adult cardiovascular system^{17,18} to construct a model of the fetal circulation and to examine the normal hemodynamic transitions during the first 24 h after birth. Build on physical and physiological principles, the CircAdapt model of the human four-chamber heart and closed-loop circulation enables fast and realistic simulation of

¹Department of Biomedical Engineering, CARIM School for Cardiovascular Diseases, Maastricht University, Maastricht, The Netherlands
Correspondence: Tammo Delhaas (tammo.delhaas@maastrichtuniversity.nl)

Received: 30 October 2020 Revised: 16 December 2020 Accepted: 21 January 2021
Published online: 17 March 2021

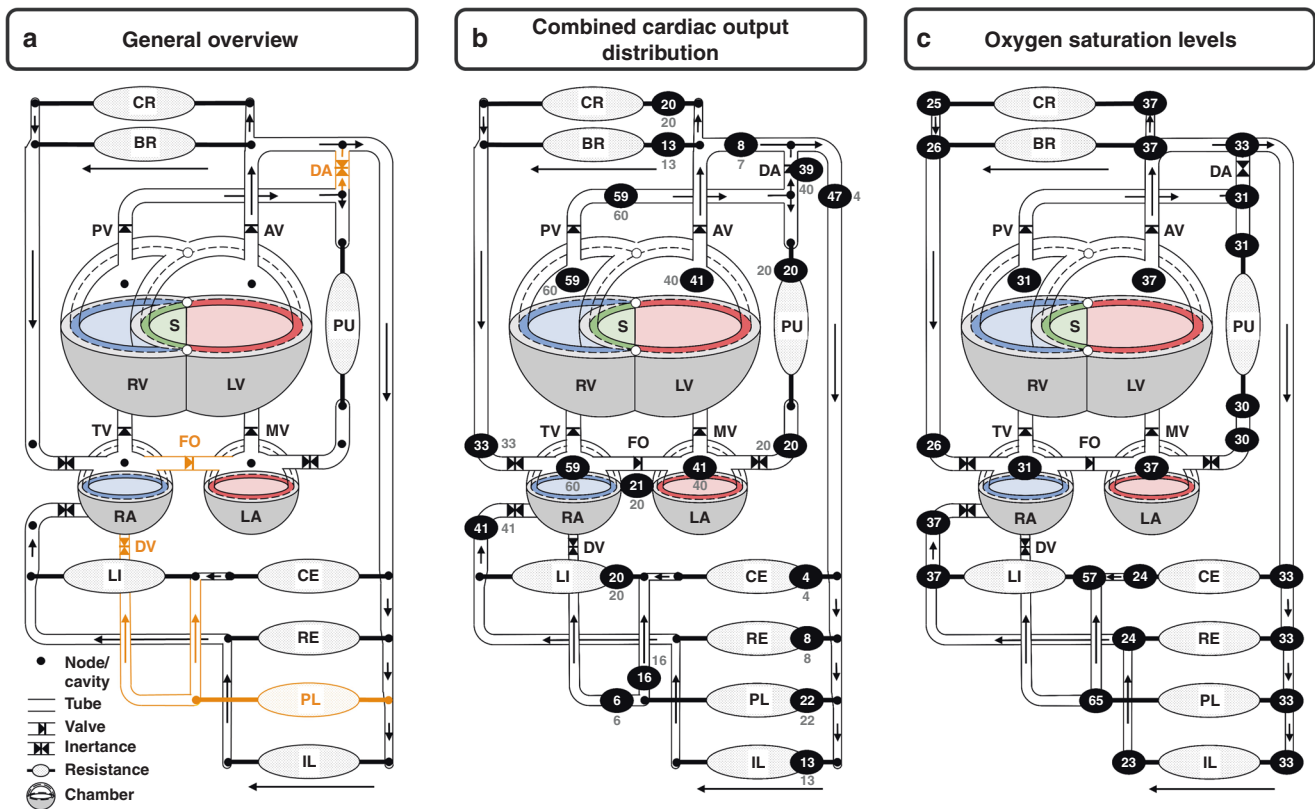


Fig. 1 The CircAdapt model of the fetal cardiovascular system with predicted combined cardiac output distribution and oxygen saturation levels. **a** In the general overview, the orange-colored tubes and valves as well as the placental arterio-venous element represent connections that close during the fetal-to-neonatal transition. Simulated cycle-averaged **b** flow rate distribution as a percentage of combined cardiac output shown in white, together with selected reference values in gray, and **c** oxygen saturation levels shown in white. The dashed line indicates the midwall volume for the left ventricle (LV) and left atrium (LA) in red, right ventricle (RV) and right atrium (RA) in blue, and septum (S) in green. The LV and RV are mechanically coupled at their junction (o). The foramen ovale (FO) was modelled as unidirectional valve, whereas the ductus arteriosus (DA) and the ductus venosus (DV) were modelled as inertias without valve leaflets. The arrows indicate the direction of flow, whereas nodes (•) indicate locations of pressure and oxygen saturation calculation. AV aortic valve, BR brachial, CE celiac, CR cerebral, DA ductus arteriosus, DV ductus venosus, FE femoral, FO foramen ovale, LA left atrium, LI liver, LV left ventricle, MV mitral valve, PL placental, PV pulmonic valve, RA right atrium, RE renal, RV right ventricle, S septum, TV, tricuspid valve.

beat-to-beat cardiovascular mechanics and hemodynamics in a wide range of physiological loading conditions and cardiovascular pathologies.^{17,19–22}

METHODS

Multi-scale cardiovascular computational model
We adapted the closed-loop CircAdapt computational model of the adult cardiovascular system^{17,18,23} (www.circadapt.org) to simulate cardiovascular mechanics and hemodynamics of the term fetal cardiovascular circulation. CircAdapt allows fast beat-to-beat simulation of the human cardiovascular system for both research and educational purposes²⁴ and has been successfully used for simulating various (congenital) cardiovascular diseases like Tetralogy of Fallot,²¹ Fontan circulation,²⁵ and pediatric pulmonary arterial hypertension.²⁶ Build on physiological and physical principles, the CircAdapt model consists of a network of modules, all representing components of the cardiovascular system, such as atrial and ventricular walls and cavities, cardiac valves, the pericardium, large blood vessels, and systemic and pulmonary circulations. Altogether, they enable real-time simulation of atrial and ventricular pressures and volumes, regional myofiber stress and strain in the cardiac walls, flow across valves, blood pressure wave propagation within the main arteries and veins, and pulmonary and systemic resistances. Mean arterial pressure (MAP) and cardiac output (CO) are regulated by adjusting the systemic peripheral resistance and total circulating blood

volume, mimicking homeostatic control mechanisms (Appendix). Detailed theoretical descriptions and validations of the various modules have been published previously.^{17,18,23} In the next few sections, we will describe the most relevant aspects of the modules used in this study.

The fetal model parameters refer to a full-term fetus, when fetal body weight and length are assumed to be ~3.5 kg and ~49 cm,²⁷ respectively, whereas the neonatal model parameters refer to a newborn infant at 24 h after birth. The level of detail in the present model (e.g., the number of vessels and organs/tissues) was chosen with the objective of describing as many clinically relevant sites of the fetal cardiovascular system as possible. Figure 1a provides a schematic representation of the modelled system.

Cardiac module

The atria and ventricles were modelled as contractile chambers with the one-fiber model, relating local myofiber mechanics to global pump mechanics under the assumption that myofiber tension is homogeneously distributed throughout the cardiac walls²⁸ (Fig. 1a). Mechanical ventricular interaction was established by force equilibrium in the junction of the three ventricular walls.¹⁸ The pericardium was modelled as a nonlinearly compliant bag.

In this study, values of ventricular tissue parameters were manually chosen so that CircAdapt reproduced experimental curves on fetal lamb myocardium^{29,30} and human fetal velocity tracings,^{31–33} as well as ventricular wall masses and dimensions of the full-term human fetus,^{34–37} indicating right ventricular dominance in utero.

Valve module

Valve pressure gradients are composed of a Bernoulli resistance and an inertial term.³⁸ Valve orifice areas of circular shape calculated from valve diameter are listed in Table 1. The mitral, tricuspid, aortic, and pulmonary valve were modelled as unidirectional valves, whereas the veno-atrial orifices as well as the ductus arteriosus (DA) and ductus venosus (DV) were modelled as open orifices introducing inertia effects and allowing bidirectional flow.

The foramen ovale (FO) was modelled as a one-way valve, assuming that it only permits right-to-left shunting.^{39,40}

Av impedance module

The terminal end of a tube was coupled to a nonlinear three-element arterial-venous (av) model, consisting of a pressure-dependent resistive wave impedance, arterial compliance, and peripheral resistance.⁴¹ An extensive description of the pulmonary and systemic resistances can be found in the Appendix.

The fetal cardiovascular model, as presented in Fig. 1a, consists of seven av elements, representing the vascular bed of tissues and organs. The upper body circulation includes the cerebral (CR; supplying the brains) and the brachial (BR; supplying the muscular tissue of the upper trunk and extremities) circulations. The lower body circulation consists of the celiac (CE; supplying the intestines), renal (RE; supplying the kidneys), hepatic (LI; supplying the liver), iliac (IL; supplying the muscular tissue of the pelvis and lower extremities), and the umbilical-placental (PL; supplying the placenta) circulations. The pulmonary circulation is represented by the av-element PU.

Parameter	Symbol	Input	Unit	Source
Cycle time	t_c	414	ms	
Mean arterial pressure	MAP	48	mm Hg	83,84
Combined cardiac output	CCO	430	mL/min/kg	86,87,90
Cerebral (CR)	q_{CR}	20	% CCO	4,85
Brachial (BR)	q_{BR}	13	% CCO	4
Celiac (CE)	q_{CE}	4	% CCO	
Renal (RE)	q_{RE}	8	% CCO	
Placental (PL)	q_{PL}	22	% CCO	4,85,86
Iliac (IL)	q_{IL}	13	% CCO	4
Hepatic (LI)	q_{LI}	20	% CCO	
Fetal resistance				
Pulmonary vascular resistance	PVR_0	8.0	mm Hg s/mL	
Systemic vascular resistance	SVR_0	2.3	mm Hg s/mL	
Oxygen consumption				
Cerebral (CR)	$VO_{2,CR}$	7.3	mL O ₂ /min	4
Brachial (BR)	$VO_{2,BR}$	4.3	mL O ₂ /min	4
Celiac (CE)	$VO_{2,CE}$	1.1	mL O ₂ /min	4
Renal (RE)	$VO_{2,RE}$	1.5	mL O ₂ /min	4
Iliac (IL)	$VO_{2,IL}$	4.3	mL O ₂ /min	4
Hepatic (LI)	$VO_{2,LI}$	4.1	mL O ₂ /min	4
Pulmonary (PU)	$VO_{2,PU}$	0.7	mL O ₂ /min	4
Umbilical venous oxygen saturation	$SO_{2,Plven}$	65	%	46–50
Cross-sectional area / diameter				
Aortic valve (AV)	$A_{open,AV}$	47 7.7	mm ² mm	78,81,90
Pulmonic valve (PV)	$A_{open,PV}$	59 8.7	mm ² mm	78,90
Mitral valve (MV)	$A_{open,MV}$	87 10.5	mm ² mm	89
Tricuspid valve (TV)	$A_{open,TV}$	92 10.8	mm ² mm	89
Foramen ovale (FO)	$A_{open,FO}$	31 6.3	mm ² mm	39,40
Ductus arteriosus (DA)	A_{DA}	20 5.0	mm ² mm	78,80,81
Ductus venosus (DV)	A_{DV}	2.0 1.6	mm ² mm	119–121

The pulmonary and systemic resistances were set to ensure the same combined CO (CCO) distribution as found in the term human fetus (Table 1).

The geometrical properties (tube lengths) of the large arteries and veins connecting the av elements to other elements or valves were based on Reymond et al.⁴² and Müller and Toro⁴³ for the adult arterial and venous segments, respectively, and were scaled according to the fetal–adult body proportions and lengths.⁴⁴

Oxygen distribution

The dynamic behavior of the CircAdapt model allows forward and backward blood flow through all cavities and vessels during the complete cardiac cycle. Mixing of blood oxygen saturation in a blood-filled cavity is determined by the in- and outflow of the cavity and their respective oxygen saturations as follows:

$$\frac{dSO_{2,cav}}{dt} = \frac{1}{V_{cav}(t)} \sum_{i=1}^n (\max(0, q_i(t))(SO_{2,i}(t) - SO_{2,cav}(t))) \quad (1)$$

with $SO_{2,cav}$ the oxygen saturation of the cavity, $SO_{2,i}$ the oxygen saturation of the inflow, q_i the blood flow rate of the inflow, and n the number of flows entering the cavity with volume V_{cav} . The preferential streaming pattern of the umbilical venous return through the DV and the FO⁴⁵ was taken into account (Appendix).

Neglecting the minor effect of dissolved oxygen, the oxygen saturation at the venous end of an av element is dependent on the oxygen consumption as follows:

$$SO_{2,ven}(t) = SO_{2,art}(t) - \frac{VO_{2,av} \times 100}{q_{av}(t) \times kO_2 \times Hb} \quad (2)$$

with $SO_{2,art}$ the oxygen saturation of the corresponding arterial cavity, $VO_{2,av}$ the oxygen consumption of the av element, q_{av} the flow across the av element, kO_2 the capacity of hemoglobin to carry oxygen (set to 1.36 mL O₂/g Hb,^{4,46}) and Hb the hemoglobin concentration in blood (set to 16 g/dL.^{4,46}) Oxygen consumption in the systemic and pulmonary tissues was derived from fetal lamb data.⁴ Oxygen uptake in the placenta was assumed to render an oxygen saturation of 65%.^{46–50}

Transitions at birth

The proposed model was controlled by a time- and event-based script of changes occurring at birth, such as lung aeration and umbilical cord clamping, as well as the changes during the transitory phase up to 24 h after birth (Table 2 and Supplementary Figure S1).

Parameter	Unit	Fetus Neonate					
		0 s	30 s	1 min	1 h	12 h	24 h
Pulmonary circulation							
r	(–)	0.0	0.5	1.0	1.0	1.0	1.0
PVR	(mm Hg s/mL)	8.0	7.8	7.6	4.7	3.3	1.8
Systemic circulation							
DAD	(mm)	5.0	5.0	5.0	3.8	0.5	0.0
MAP_t	(mm Hg)	48.0	48.0	48.0	48.5	54.0	60.0
q_{sys}	(mL/min/kg)	250	250	250	250	250	250
$VO_{2,sys}$	(mL O ₂ /min)	22.6	22.6	22.6	22.6	22.6	22.6
Placental circulation							
q_{pl}	(mL/min/kg)	94.0	0.0	0.0	0.0	0.0	0.0
$SO_{2,plven}$	(%)	65.0	0.0	0.0	0.0	0.0	0.0

Lung aeration. With the onset of breathing, blood is being oxygenated in the lungs. The rise in oxygen saturation at the venous end of the pulmonary av element (PUven) ($SO_{2,PUven}$) was described as:

$$\frac{dSO_{2,PUven}}{dt} = \frac{1}{V_{PUven}(t)} (r(t) \max(0, q_{PU}(t)) (0.98 - SO_{2,PUven}(t)) + \min(0, q_{PUvenLA}(t)) (SO_{2,PUven}(t) - SO_{2,LA}(t))) \quad (3)$$

With r a function describing the fraction of pulmonary blood flow (PBF) that is saturated, V_{PUven} the volume of the venous pulmonary cavity (PUven), q_{PU} the flow through the pulmonary av element (PU), $SO_{2,LA}$ the oxygen saturation of the left atrium (LA), and $q_{PUvenLA}$ the retrograde flow from the LA into the pulmonary vein. Note that the pulmonary oxygen uptake is set to render a pulmonary venous oxygen saturation of 98%.⁵¹ The function $r(t)$ in Eq. (4) increases linearly from zero at the onset of breathing to one when the lungs are fully aerated:

$$r(t) = \begin{cases} 0 & \text{if } t < t_0 \\ \frac{t-t_0}{t_s} & \text{if } t_0 \leq t \leq t_s \\ 1 & \text{else} \end{cases} \quad (4)$$

with t_0 the onset of breathing and t_s the time it takes to achieve fully aerated lungs. The value of t_s was set to 1 min, based on pre- and post-ductal oxygen saturation levels measured in the first minute after birth.^{52–61}

After birth, lung aeration immediately triggers the decrease in pulmonary vascular resistance (PVR) and increase in PBF.⁶² The initial rapid decrease in PVR is followed by a more gradual decline over the following days and weeks.^{63,64} An estimated reduction in PVR of 74% was reported after the start of ventilation in lambs.⁶⁵ Based on lamb PVR^{4,5,65} and pulmonary arterial pressure data,^{66–68} an exponential function was followed by a linear function to mimic the initial rapid decrease in the first 36 min after birth and the more gradual decline in PVR thereafter:

$$PVR(t) = \begin{cases} PVR_0(1 - 0.42(1 - e^{-8t})) & \text{if } 0 \leq t \leq 36 \text{ min} \\ PVR_0(0.58 - 0.016(t - 0.6)) & \text{if } 36 \text{ min} < t \leq 12 \text{ h} \\ PVR_0(0.41 - 0.0062(t - 12)) & \text{if } 12 \text{ h} < t \leq 24 \text{ h} \end{cases} \quad (5)$$

with PVR_0 the PVR in the full-term fetus.

Cord clamping. Thirty seconds after birth, umbilical vascular resistance was instantly increased to infinity, mimicking umbilical cord clamping.

DA closure. After birth, the DA gradually constricts, with functional closure occurring between 12 and 48 h after birth in the majority of newborn infants.^{69–77} Based on DA diameter (DAD) data from several studies,^{72–74,78,79} an exponential function was formulated to mimic the gradual constriction:

$$DAD(t) = \frac{1}{2} DAD_0 \times e^{-0.43t} + \frac{1}{2} DAD_0 \times e^{-0.14t} \quad (6)$$

with DAD the diameter in meters and t the time in hours. The diameter before birth (DAD_0) was set to 0.0050 m.^{78,80,81} The resistance (DAR) was calculated under the assumption of Poiseuille flow:

$$DAR(t) \cong \frac{1}{DAD^4(t)} \quad (7)$$

Mean arterial pressure. The gradual increase in MAP that occurs after birth was modelled with a linear function:

$$MAP(t) = \left(\frac{MAP_t - MAP_0}{24} \right) t + MAP_0 \quad (8)$$

with t the time in hours, and MAP_0 and MAP_t the reference and target MAP (Appendix), which were set to 48 and 60 mm Hg, respectively.^{66,73,82–84}

Simulation protocol

Cardiac cycle length was set to 0.414 s (heart rate of 145 beats/min). Absolute flow and oxygen consumption of the systemic elements were kept the same throughout the entire fetal-to-neonatal transition, even with loss of umbilical venous return (Supplementary Figure S2). After DA closure at 24 h after birth, left ventricle (LV) and right ventricle (RV) are forced to act in series and, hence, to deliver an output of 250 mL/min/kg each. Major input parameter values are presented in Table 1.

Numerical implementation

The set of differential equations describing pressure, volume, and oxygen saturation were solved with a time step of 0.1 ms. All simulations were implemented in MATLAB 2019a (The MathWorks, Natick, MA) on a standard personal computer with an Intel® Core™ i7 processor and 16 GB RAM.

RESULTS

Validation

For the validation of the model, simulated CCO and distribution, oxygen saturations, intra-cardiac, and arterial blood pressures, as well as flow velocity waveforms, were compared to target data. Target data were obtained from healthy infants before and after birth, as well as from animal experiments, in case human data were lacking. The next few sections (and Tables 1 and 3) give an overview of the key findings. A more extensive description of the results as well as a comparison of input and output values with target data can be found in Supplemental Material.

Fetal endpoint

Figure 1b shows the simulated flow rate distribution as a percentage of CCO, together with selected reference values for direct comparison. The systemic and pulmonary resistances were set to ensure the same CCO distribution as found in the human term fetus.^{4,78,80,85–87} Simulated right-to-left output ratio was 1.4, corresponding well with the reported range 1.0–1.5.^{30,33,78,80,87–93}

Simulated oxygen saturation levels in the term fetus are shown in Fig. 1c. Due to the scarcity of in utero human fetal blood oxygen saturation measurements, validation of oxygen saturation levels was restricted to umbilical saturation levels obtained in newborn infants directly after birth. Umbilical arterial oxygen saturation of 33% is within 1 SD of human newborn target data^{46–50} (Table 3). The higher oxygen saturation level in the LV compared to the RV (LV: 37%; RV: 31%, is caused by the abundant volume of oxygenated umbilical blood presented to the FO.⁴ As a consequence, pre-ductal oxygen saturation levels exceed post-ductal oxygen saturation levels.

Simulated and measured⁹⁴ flow velocity waveforms of the fetal shunts are presented in Fig. 2. Simulated cardiac and vascular pressure waveforms, as well as flow velocity waveforms across the cardiac valves and volumic changes of the fetal cardiac chambers, are shown in Fig. 3a. Both ventricular SV (LV: 4.3 mL; RV: 6.1 mL) and ejection fraction (LV: 63%; RV: 53%) correspond well with clinical values,^{35–37,78,87,90,95} although RV values are slightly lower than reported values (Table 3). An explanation can be attributed

Table 3. Major output parameter values for the fetal circulation.

	Unit	Literature		Simulation
		Ref.	Value	
Cardiac output				
Left ventricle	mL/min	86	476	625
		87	554	
		78	912	
		89	820	
Right ventricle	mL/min	86	950	887
		87	953	
		78	1165	
		89	915	
Stroke volume				
Left ventricle	mL	87	4	4.3
		78	5.7	
		90	5.2	
Right ventricle	mL	87	7	6.1
		78	8.5	
		90	7.6	
Ejection fraction				
Left ventricle	%	35	62	63
		36	60	
		95	67	
Right ventricle	%	35	52	53
		36	55	
		95	66	
Atrial pressure				
Mean left atrial pressure	mm Hg	75	3.4	4.5
Mean right atrial pressure	mm Hg	75	3.7	4.6
Systemic arterial pressure				
Diastolic arterial pressure	mm Hg	83	38	38
		83	39	
Mean arterial pressure	mm Hg	84	45	48 ^a
		83	48	
		83	48	
Systolic arterial pressure	mm Hg	83	64	61
Pulse pressure	mm Hg	84	29	23
		84	26	
Pulmonary arterial pressure				
Mean pulmonary arterial pressure	mm Hg	99 ^b	49	49
		5 ^c	53	
		68 ^d	48	
Umbilical pressure				
Mean umbilical venous pressure	mm Hg	22	6.5	6.5
		113	5.3	
Mitral valve				
A peak velocity	m/s	96	0.42	0.39
		31	0.52	
		32	0.36	
		2	0.40	
E peak velocity	m/s	96	0.34	0.37
		31	0.41	
		32	0.31	
		2	0.32	
A/E ratio	-	2	1.26	1.07
E/A ratio		96	0.81	0.91
		31	0.91	
		32	0.86	

Table 3. continued

	Unit	Literature		Simulation
		Ref.	Value	
Tricuspid valve				
A peak velocity	m/s	96	0.50	0.51
		31	0.63	
		2	0.45	
E peak velocity	m/s	96	0.38	0.46
		31	0.51	
		2	0.35	
A/E ratio	-	2	1.31	1.10
E/A ratio		96	0.75	0.93
		31	0.82	

^aMean arterial cardiac output is maintained due to homeostatic control mechanisms implemented in the CircAdapt model.

^bPlacental oxygen uptake equals the total oxygen consumption with a birth weight of 3.5 kg.

^cOxygen consumption in the late-gestation fetal lamb, downscaled to match the placental oxygen consumption in the term human fetus.

^dAssuming equal distribution between brachial and femoral circulations.

from various timings in gestational age in the reported measurements together with a general decrease in RV dominance and increase in PBF during the last trimester.⁴ In our study, pulmonary flow fraction (20%) and right-to-left shunting across the FO (21%) correspond with a full-term fetus, and hence may differ from reported measurements, explaining the slightly lower RV values.

Simulated E and A wave velocities of mitral (E: 0.37 m/s; A: 0.39 m/s) and tricuspid (E: 0.46 m/s; A: 0.51 m/s) valve were in agreement with clinical observations in the healthy term fetus^{2,31,32,96} (Table 3). The wide variation found in reported values can be explained by differences in e.g. gestational age, CO, heart rate, orifice area, and fetal breathing movements, as well as by the relatively small data sets.

Data regarding fetal cardiac and vascular pressures is limited due to the extremely high invasiveness of the measurements. However, both simulated mean atrial (LA: 4.5 mm Hg; RA: 4.6 mm Hg) and MAPs (aorta: 48 mm Hg (set); pulmonary: 49 mm Hg) are within 1 SD of human⁹⁷ and animal⁹⁸⁻¹⁰¹ target data.

The high resistance ratio between the pulmonary and systemic circulation is reflected in the direction of flow through the DA, with continuous right-to-left shunting^{6,102,103} (Fig. 4a). This provides the pulmonary arterial blood flow waveform with unique characteristics in utero; pulmonary arterial blood flow is directed towards the lungs during most of the systole, yet away from the lungs throughout diastole (Fig. 4a).¹⁰⁴ This phenomena is consistent with fetal lamb data.^{6,105}

Lung aeration

An overview of the simulated model parameter changes and evolution of the modelled resistances, flow rates, pressures, and oxygen saturation levels from the fetus to the 24-h-old neonate are presented in Fig. 5, together with target data for direct comparison. With the onset of breathing, the PVR starts to decrease (Fig. 5a), resulting in a gradual increase in PBF (Fig. 5c). As lung aeration causes oxygenation of pulmonary venous blood, oxygen saturation levels considerably increase (Fig. 5e).

Umbilical cord clamping

With the clamping of the umbilical cord, loss of the low-resistance placental bed primarily leads to ① an immediate increase in systemic vascular resistance (SVR) of ~0.90 mm Hg s/mL (Fig. 5a), ② a decrease in LV CO, RV CO, and CCO of ~ 26%, 28%, and 27%,

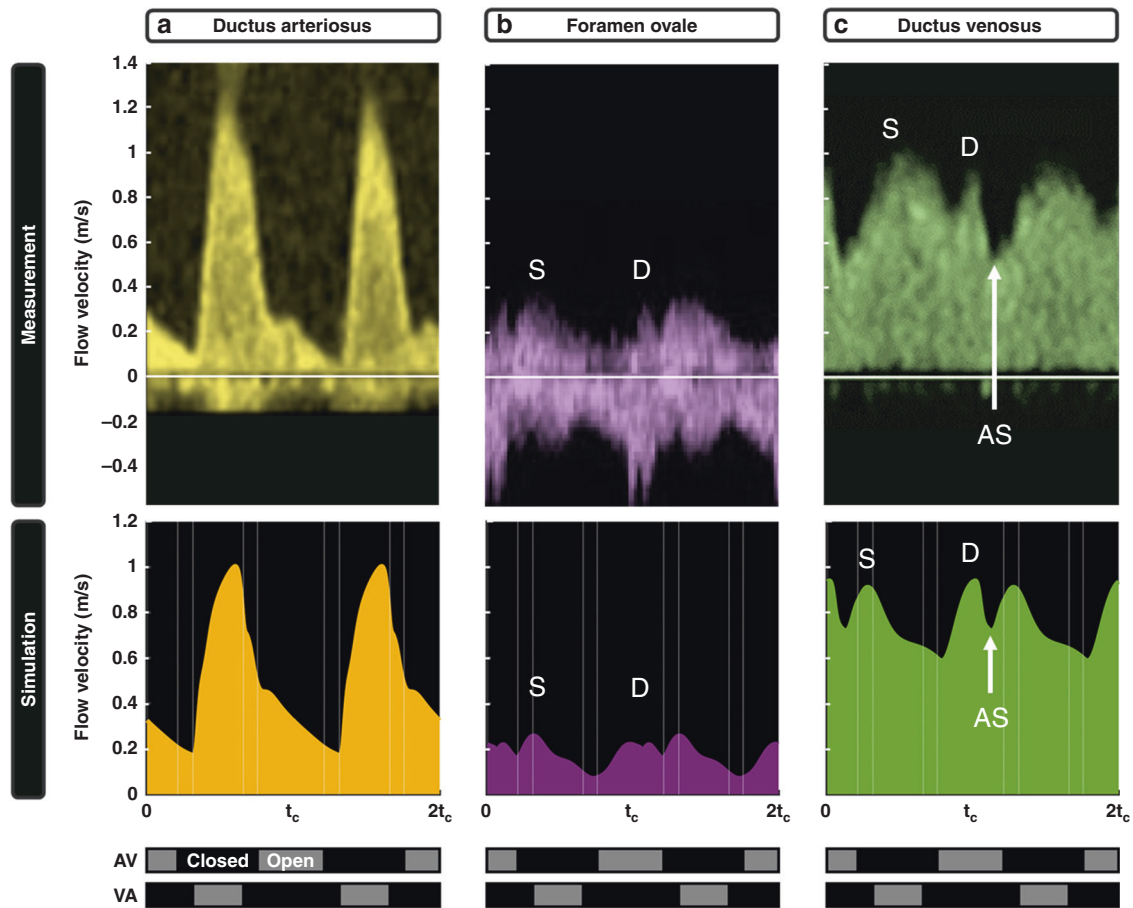


Fig. 2 Measured (top row) and simulated (bottom row) fetal shunt flow velocity waveforms. Fetal shunt flow velocity waveforms of the **a** ductus arteriosus, **b** foramen ovale, and **c** ductus venosus for two consecutive heartbeats with cycle time t_c . Vertical dashed lines and horizontal black/gray bars indicate opening and closing of the left atrioventricular (AV) and ventriculo-arterial (VA) cardiac valves. AS atrial systole, D peak during diastole, S peak during systole. Doppler waveforms adapted from Shah et al.⁹⁴

respectively (Fig. 5b), and ③ a brief decay in pre- and post-ductal oxygen saturation (Fig. 5e).

① The decrease in PVR and increase in SVR lead to a decrease in the pressure gradient between the pulmonary and systemic circulation (Fig. 4b). As a consequence, right-to-left DA flow decreases.

② Atrial and ventricular pressure–volume curves are displayed in Fig. 6. As venous return is not yet restored at 1 min after birth, both RV and LV show a lower workload with an SV of 4.5 mL (fetus: 6.1 mL) and 3.3 mL (fetus: 4.3 mL), respectively.¹⁰⁶

③ With the onset of breathing before umbilical cord clamping and rise in PBF, the sudden loss of oxygen uptake in the placenta is replaced within a minute by the oxygen uptake in the lungs (Fig. 5e). Time to reach 90% was ~6.7 and 9.6 min for the pre- and post-ductal sites, respectively.^{52–61} Pre- and post-ductal sites reached normal adult value (98%) at ~12 and 15 min after birth, respectively.^{52,54,57}

Transitory phase (and ductus arteriosus closure)

DA flow becomes bidirectional at ~10 min after birth and mainly left-to-right shortly thereafter (Fig. 5c), due to the continuous decrease in PVR (Fig. 5a). The reversed DA flow is counter-productive, forming a short-circuit loop from the LV to the LA through the pulmonary circulation. FO flow meanwhile decreases (Fig. 5c), due to rising LA pressure, with functional FO closure occurring at 15 min after birth. Hence, LA and LV workload considerably increases (LV SV, 1 h: 8.7 mL; fetus: 4.3 mL), whereas RV workload remains fairly similar to that in the fetus (RV SV, 1 h: 6.0 mL; fetus: 6.1 mL) (Fig. 6).

From 1 h after birth, LV output decreases (Fig. 5b), due to the rise in DA resistance (Fig. 5a) and, hence, decrease in PBF. Furthermore, the difference between aortic and pulmonary arterial pressure increases (Fig. 4e), with mean pulmonary arterial pressure 50% of mean aortic pressure at 24 h after birth (Fig. 5d).⁶⁶

The pressure, flow velocity, and volume waveforms of the left- and right-sided heart for the neonatal endpoint are displayed in Fig. 3b. The decreased A/E ratio for the mitral valve (fetus: 1.07; 24 h: 0.82) and relatively unchanged A/E ratio for the tricuspid valve (fetus: 1.10; 24 h: 1.12) agree with reported values in healthy neonates at 24 h after birth (mitral valve: 0.79; tricuspid valve: 1.12).¹⁰⁷

Decreased mean pulmonary arterial pressure (fetus: 49 mm Hg; 24 h: 30 mm Hg) at near-constant RV output resulted in a leftward shift in its pressure–volume curve (Fig. 6). For the LV, the increase in mean aortic pressure (1 h: 49 mm Hg; 24 h: 60 mm Hg) and decrease in PBF contribute to a substantial decrease in workload (LV SV, 1 h: 8.7 mL; 24 h: 6.0 mL).

DISCUSSION

The CircAdapt computational model of the adult cardiovascular circulation was adapted to simulate the fetal circulation as well as its transition to the cardiovascular system of a 24-h-old neonate. Although many mathematical models have been developed to describe the fetal circulation^{9–16} or the cardiovascular fetal-to-neonatal transition,^{7,8} they often lack oxygen saturation levels, homeostatic control mechanisms, phasic hemodynamic signals, or describe the heart with a time-

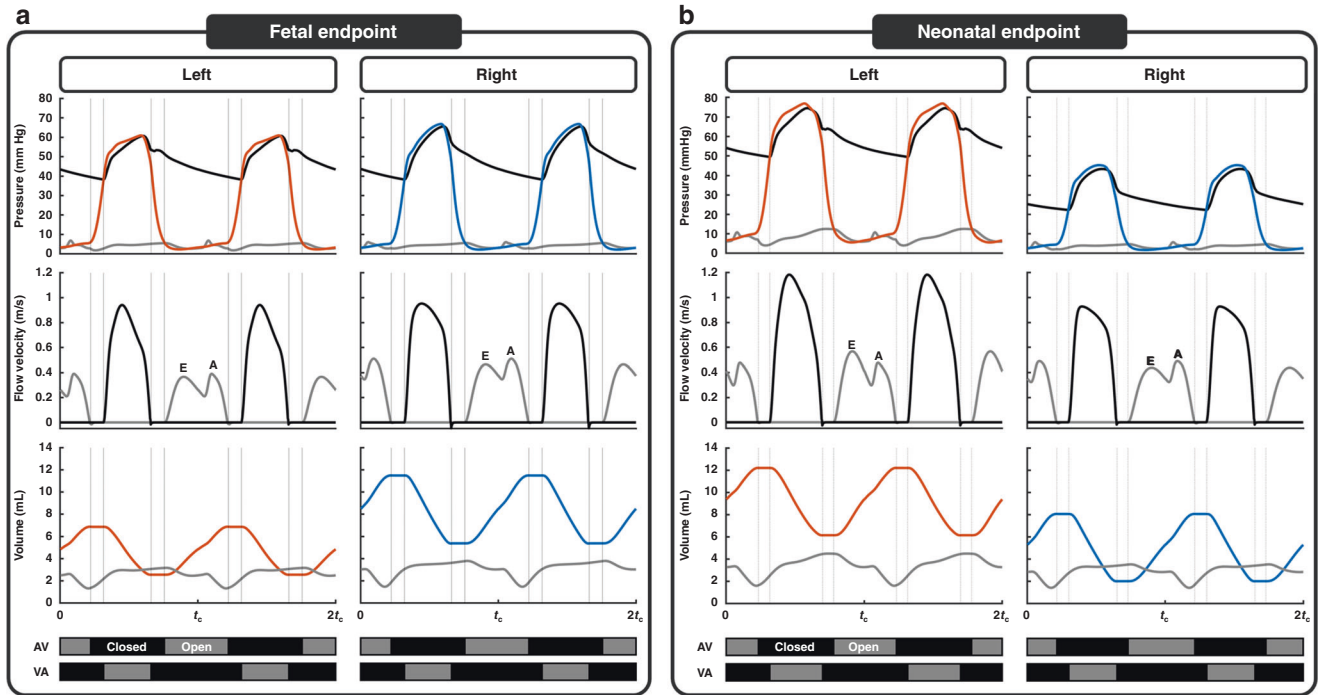


Fig. 3 Simulated pressure, flow velocity, and volume waveforms for the fetal and neonatal endpoint. **a** Fetal endpoint refers to the term human fetus, whereas **b** neonatal endpoint refers to the 24-h-old neonate when the ductus arteriosus is closed. Simulated waveforms for pressure (top), flow velocity (middle), and volume (bottom) are shown for two consecutive beats with cycle time t_c of the left (left panel) and right (right panel) side of the heart. Left ventricular pressure and volume are shown in red, whereas right ventricular pressure and volume are shown in blue. Atrial pressure and volume, as well as atrioventricular flow, are shown in gray. Arterial pressure and ventriculo-arterial flow are shown in black. Vertical dashed lines and horizontal black/gray bars indicate opening and closing of the atrioventricular (AV) and ventriculo-arterial (VA) valves of the corresponding left or right side. E and A denote the early and atrial activation waves of the atrioventricular flow velocity waveform.

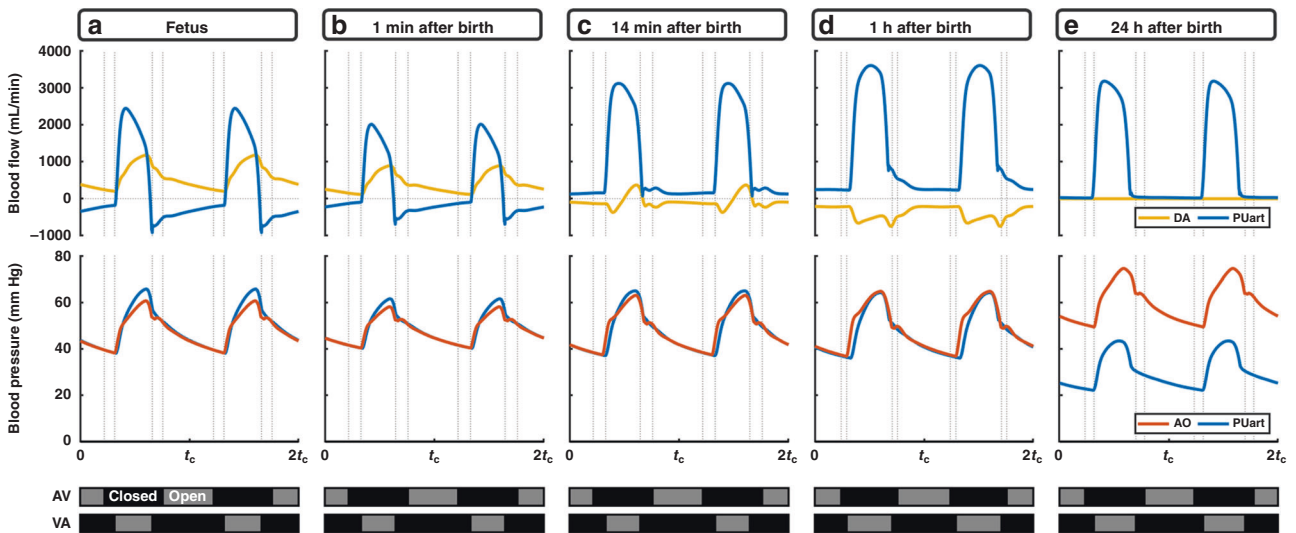


Fig. 4 Simulated blood flow waveforms in the ductus arteriosus (DA) and pulmonary artery (PUart) and pressure waveforms in the aorta (AO) and pulmonary artery (PUart). Waveforms shown for two consecutive heartbeats with cycle time t_c in **a** the fetus, and **b** 1 min, **c** 14 min, **d** 1 h, and **e** 24 h after birth. Vertical dashed lines and horizontal black/gray bars indicate opening and closing of the left atrioventricular (AV) and ventriculo-arterial (VA) cardiac valves.

varying elastance model. In this study, we identified relevant changes in flow velocity and pressure waveforms, as well as the distributions of blood flow and oxygen saturation levels throughout the cardiovascular system, while mimicking homeostatic pressure-flow control mechanisms.

Fetal endpoint

High mean flow velocity in the DV. In utero, the majority of the blood effectively bypasses the lungs by right-to-left shunting across the DA and FO, with the majority of the FO blood flow coming from DV blood flow.¹⁰⁵ In our simulations, the large

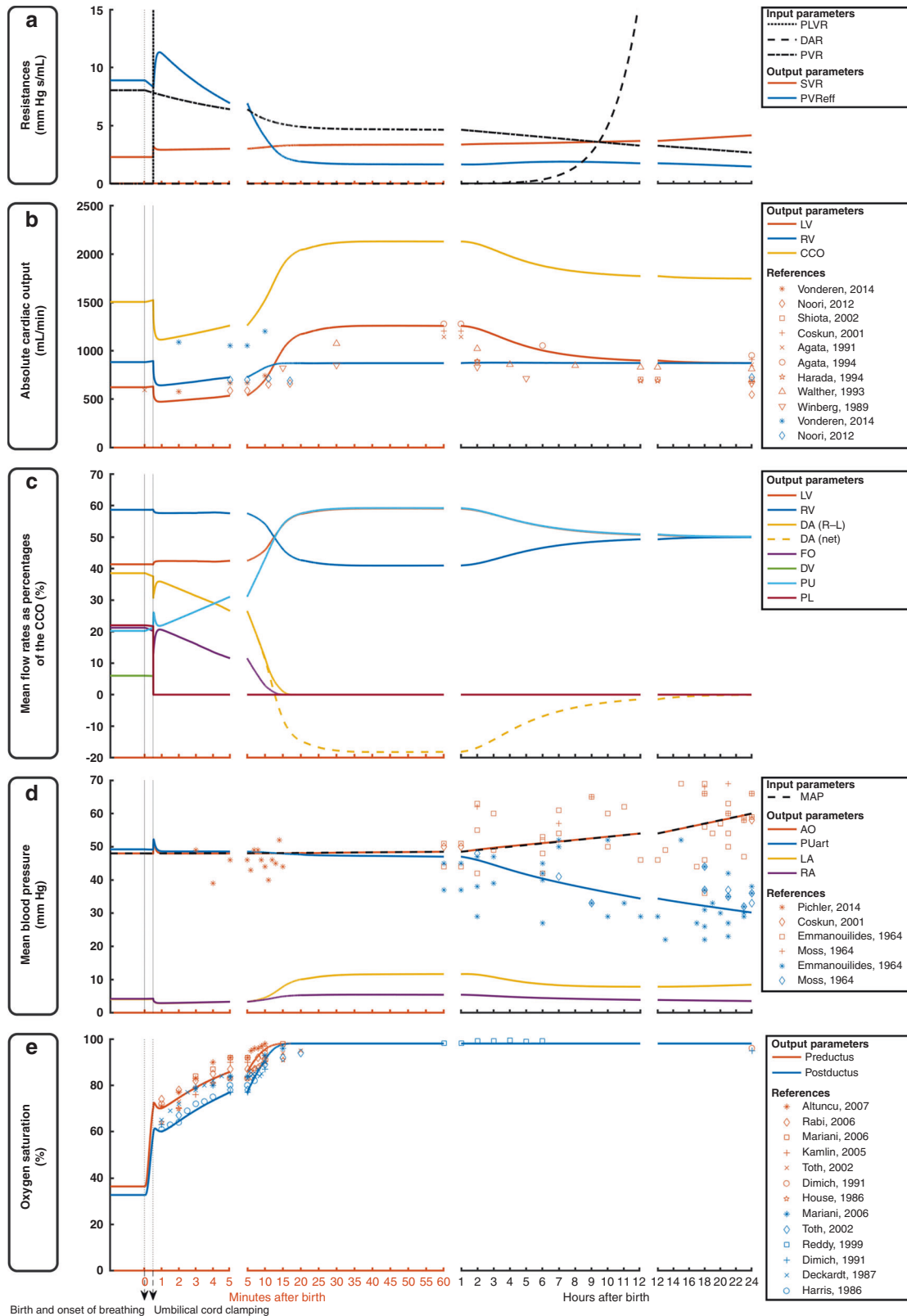


Fig. 5 Simulated model input (black lines) and output (colored lines) parameter changes and direct comparison with clinical data (markers) for the first 24 h after birth. Included parameters are **a** resistance, **b** absolute cardiac output, **c** mean blood flow as a percentage of the combined cardiac output, **d** mean blood pressure, and **e** oxygen saturation. AO aorta, CCO combined cardiac output, DA (net) net ductus arteriosus shunting, DA (R-L) ductus arteriosus right-to-left shunting, DAR ductus arteriosus resistance, DV ductus venosus, FO foramen ovale, LA left atrium, LV left ventricle, MAP mean arterial pressure, PL placental arterio-venous element, PUart arterial end of the pulmonary arterio-venous element PU, PVR pulmonary vascular resistance, PVR_{eff} effective pulmonary vascular resistance, RA right atrium, RV right ventricle, SVR systemic vascular resistance.

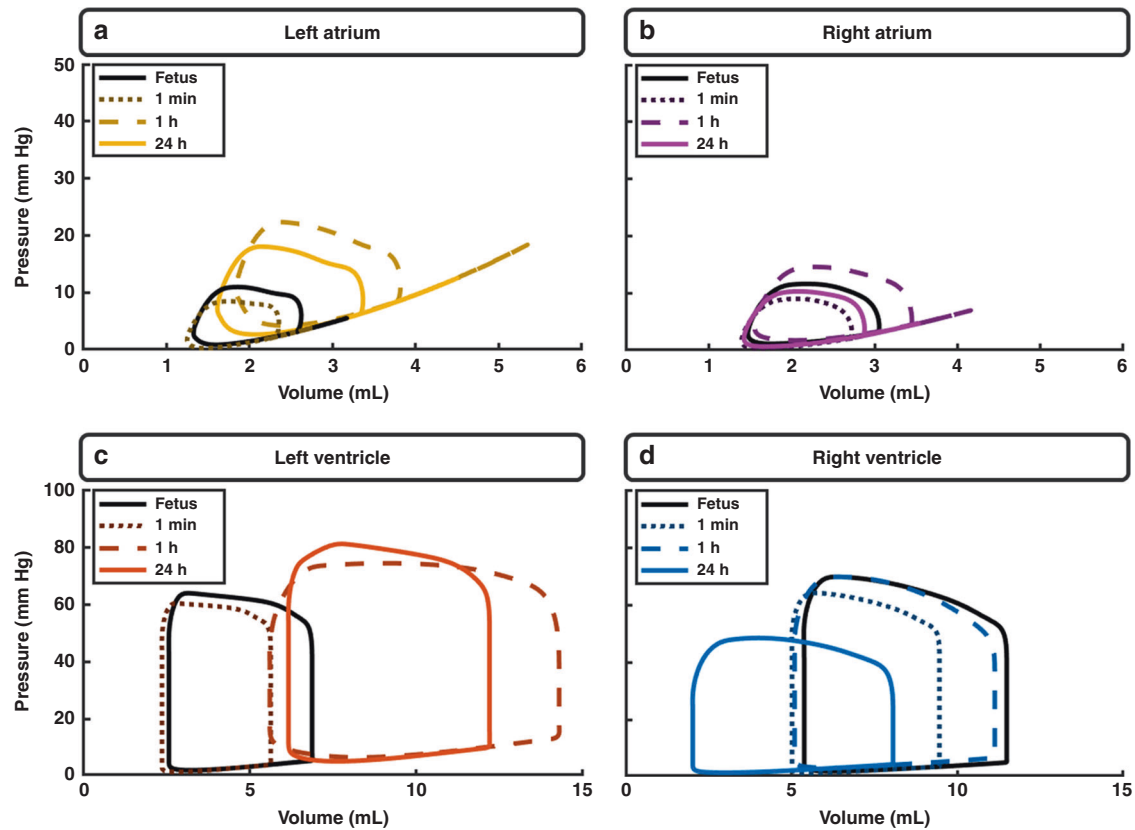


Fig. 6 Simulated atrial and ventricular pressure-volume loops at different time points during the transition. Simulated pressure–volume loops of the **a** left atrium, **b** right atrium, **c** left ventricle, and **d** right ventricle in the fetus, as well as 1 min, 1 h, and 24 h after birth.

pressure drop across the DV and the substantially smaller DV cross-sectional area, compared to the DA and FO cross-sectional areas, contribute to the high mean flow velocity (Fig. 2). We hypothesize that this high kinetic energy enables blood to preferentially pass through the FO.

Inverted mitral and tricuspid flow patterns. In contrast to what is normally found in the adult, the fetal atrioventricular waveform is characterized by a late filling peak (A wave) that is higher than the early filling peak (E wave). Reed et al.² reported an A/E ratio for the tricuspid valve of 1.20 ± 0.12 at 36–39 weeks gestation (1.10 in our model) and an A/E ratio for the mitral valve of 1.11 ± 0.17 at 36–39 weeks gestation (1.07 in our model) (Fig. 3a).²

Vasoconstriction of fetal vessels

With umbilical cord clamping taking place at 30 s after birth, arterial oxygen saturations showed a brief drop of ~3% caused by loss of the relatively high umbilical venous oxygen saturation and flow rate (Fig. 5). However, the onset of breathing and corresponding increase in arterial oxygen partial pressure may facilitate gradual umbilical arterial constriction, with the cessation of umbilical arterial flow usually within 45 s after birth.^{108,109} We neglected these effects to achieve a simpler model. The rise in arterial oxygen saturation, furthermore, promotes DA constriction,^{75–77} which is mimicked with an exponential function in our simulation. Hence, implementing vasoconstriction upon increases in arterial oxygen saturation may slightly change blood flows as well as oxygen saturation levels and would additionally allow for the simulation of, for example, delayed cord clamping.

Postnatal time to reach oxygen saturation $\geq 90\%$ is >5 min. In agreement with observational studies,^{52–61,110} our simulation demonstrates that newborns remain poorly saturated immediately

after birth, and that, although oxygen saturation levels improve steadily, normal adult values are not to be expected within the first 15 min after birth. Several studies reported time to reach an oxygen saturation $\geq 90\%$ of >5 min,^{52–54,56–59} with slightly longer times for post-ductal sites due to right-to-left shunting. The combination of persistent right-to-left atrial and DA shunting, and ventilation–perfusion mismatching most likely explain the inability to saturate arterial blood with oxygen in the first minute after birth.

Increased preload of the left ventricle in the early neonatal period. The simulation showed a decrease in CO with umbilical cord clamping, DA-induced temporal increase in LV output afterwards (LV output, fetus: 623 mL/min; 30 min: 1259 mL/min), as well as a gradual decrease from 1 h onwards. Various studies showed similar trends,^{71,73,79,82,106,111–113} although magnitudes may vary. With heart rate not significantly changed, a combination of increased PBF and a widely patent DA with predominantly left-to-right shunting likely explains the two-fold increase in LV output at 30 min after birth. Hence, the neonatal heart is working at a relatively high level of the Frank–Starling curve in the early neonatal period.

Limitations and future work

Potential limitations of this simulation may result from the lack of sufficient human physiological and experimental data to compare simulation results with target data. This lack of sufficient data is, for example, prominent in our assumption on constant oxygen consumption as well as the homeostatic pressure–flow regulation and FO valve function given their relatively crude way of modelling. PBF may be underestimated in our model due to the lack of LA volume overload-induced left-to-right FO shunting. Despite the use of animal data for the decline in PVR, the simulation results provide a good approximation of the transitory

phase in different parts of the simulation. Other limitations may arise from the timing of umbilical cord clamping as well as lack of amnion fluid resorption and biomechanical responses at birth.

Future work will include expansion of the model with vasoconstriction and vasodilatation upon changes in arterial oxygen saturation levels as well as left-to-right atrial shunting due to LA volume overload. Incorporation of congenital heart disease or pathologies that may occur during the transitional period will further enhance this model's potential educational and scientific research impact. The current version of the CircAdapt model and educational simulation tool can be downloaded free of charge from www.circadapt.org.

CONCLUSION

The CircAdapt model of the adult cardiovascular circulation was adapted to simulate the hemodynamics of the fetal circulation and the fetal-to-neonatal transition. Simulation results were validated using experimental and clinical data. Fetal and neonatal endpoints, as well as the events occurring during and directly after birth and the transition during the first 24 h after birth, were realistically represented. The model can, therefore, be used as an educational tool to demonstrate the hemodynamics of the complex fetal circulation and fetal-to-neonatal transition. Furthermore, it can serve as a research platform for in silico investigation of fetal-to-neonatal hemodynamic changes under pathological conditions, for example, in the presence of congenital heart diseases.

ACKNOWLEDGEMENTS

J.L. was funded through the Netherlands Organisation for Scientific Research (NWO-ZonMw, VIDI grant 016.176.340) and the Dutch Heart Foundation (grant 2015T082).

AUTHOR CONTRIBUTIONS

A.G.M. participated in the conception, design, and analysis of the data; all authors participated in the drafting of the manuscript, revising it critically, and final approval of the submitted manuscript.

ADDITIONAL INFORMATION

Supplementary information The online version contains supplementary material available at <https://doi.org/10.1038/s41390-021-01401-0>.

Competing interests: The authors declare no competing interests.

Publisher's note Springer Nature remains neutral with regard to jurisdictional claims in published maps and institutional affiliations.

APPENDIX

Pulmonary and systemic resistances

The CircAdapt model consists of a four-chamber heart connected to a closed-loop cardiovascular system, with lumped pulmonary and systemic circulations. Assuming that the peripheral flow depends on the cross-sectional area via the Hagen–Poiseuille equation,¹¹⁴ the peripheral flow (q_{av}) can be related to the av pressure drop (Δp_{av}) as follows:

$$q_{av}(t) = q_{av,0} \left(\frac{|\Delta p_{av}(t)| V_{av}^2(t)}{\Delta p_{av,0} V_{av,0}^2} \right)^{k_{av}} \text{sgn}(\Delta p_{av}(t)) \quad (\text{A1})$$

with the subscript 0 referring to the reference situation, and V_{av} the volume of the av element. The signum function (sgn) extracts the sign of the av pressure drop (Δp_{av}), thereby determining whether the blood flows forward or backward through the av element.

In the CircAdapt model, $q_{av,0}$ is always held constant, whereas $\Delta p_{av,0}$ can be changed between cycles in the homeostatic pressure-flow control described in a section below. Hence, changing $\Delta p_{av,0}$ changes the av vascular resistance. Intuitively,

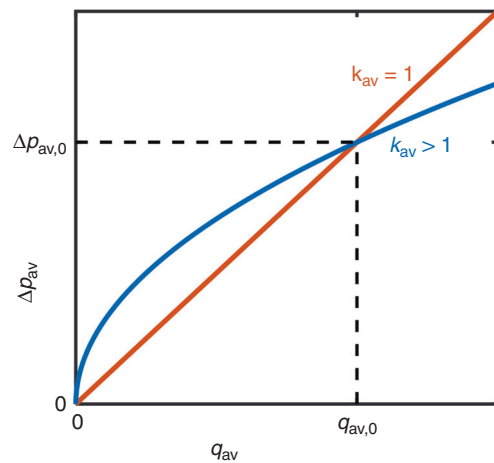


Fig. 7 (Non-)linear pressure-flow relation for the arterio-venous (av) resistance, assuming the volume term in Eq. (A1) is constant. The nonlinearity of the pressure-flow relation is determined by the exponent k_{av} . A linear relation ($k_{av} = 1$) was assumed for all systemic elements, due to homeostatic control mechanisms. The relation becomes nonlinear for higher k_{av} values. A nonlinear relation ($k_{av} = 2$) was assumed for the pulmonary element, due to vessel dilation and/or vessel recruitment in the pulmonary circulation. The setpoint for the peripheral resistance is determined by the reference av pressure drop ($\Delta p_{av,0}$) and flow rate ($q_{av,0}$). Note that the nonlinear pulmonary peripheral resistance increases with a decrease in current pulmonary flow rate (q_{av}).

$\Delta p_{av,0}$ can be seen as the pressure difference between the av artery and vein that would be required to generate a constant systemic flow of $q_{av} = q_{av,0}$.

Although the reference av pressure drop ($\Delta p_{av,0}$) and flow ($q_{av,0}$) determine the setpoint for the peripheral resistance, the nonlinearity of the pressure-flow relation is determined by the exponent k_{av} (Fig. 7). The pressure-flow relation is set to be linear ($k_{av} = 1$) for all systemic av elements. The PVR, however, is presumed to fall nonlinearly ($k_{av} = 2$) with increases in PBF, due to vessel dilation and/or vessel recruitment in the pulmonary circulation.^{115–118}

The high PVR in utero was established by using an increased reference pulmonary av pressure drop ($\Delta p_{PU,0} > \Delta p_{PU}$), thereby reducing the pulmonary av flow rate ($q_{PU} < q_{PU,0}$) (Fig. 7). With the systemic flow maintained by homeostatic pressure-flow control mechanisms ($q_{av} = q_{av,0}$), the reduced pulmonary flow ($q_{PU} < q_{PU,0}$) inherently reduces the CCO ($CCO < CCO_0$). Hence, the reference pulmonary av pressure drop ($\Delta p_{PU,0}$) was increased to 117 mm Hg, while keeping the reference pulmonary av flow rate ($q_{PU,0}$) at 50% of the neonatal CCO of 500 mL/min/kg, thereby reducing the simulated pulmonary flow rate (q_{av}) to 20% of the fetal CCO of 430 mL/min/kg. The remainder of the CCO was divided among the systemic elements (Table 1).

Homeostatic pressure-flow control

In the CircAdapt model, homeostatic pressure-flow control is used to maintain a reference CO ($q_{sys,0}$) and reference mean systemic arterial pressure (MAP_0). Note that q_{sys} is not necessarily the same as $q_{sys,0}$ in Eq. (A1). In the current study, MAP_0 is set to 48 mm Hg for the fetus, and increases linearly after birth to 60 mm Hg at 24 h.

The homeostatic pressure-flow control represents two physiological processes; acutely, it represents the recruitment of pooled blood in the venous system into the circulating blood volume, whereas in the longer term, it represents the renin–angiotensin–aldosterone system (RAAS) on fluid retention to maintain CO.

With homeostatic pressure-flow control enabled, CircAdapt calculates the ratio between current mean systemic arterial pressure over the cardiac cycle ($MAP = \bar{p}_{aorta}$) and MAP_0 at the end of each cardiac cycle. This ratio is then used to incrementally alter the av vascular resistance through changes in $\Delta p_{av,0}$, with the process repeated over multiple cardiac cycles until $MAP = MAP_0$

$$\Delta p_{av,0,new} = \left(\frac{MAP_0}{MAP} \right)^a \left(\frac{q_{av}}{q_{av,0}} \right)^a \Delta p_{av,0,old}$$

with $a < 1$ a damping factor that prevents oscillatory behavior. Hence, the av vascular resistance will increase when MAP is too low, and decrease when av flow (q_{av}) is too low. One must bear in mind that the pressure-flow control is only applied to systemic av elements, the PVR remains unaffected.

To represent RAAS and/or fluid retention of pooled blood, the circulating blood volume alters with the SVR by injecting or removing volume per cardiac cycle into the cardiac system from the systemic bed, that is, by altering the flow entering the

systemic veins (q_{ven}), so that

$$q_{ven}(t) = \left(\frac{MAP_0}{MAP} \right)^a q(t)$$

with q the flow across the systemic circulation. Note that $MAP_0 > MAP$ represents recruitment of pooled blood into the circulation or fluid retention by RAAS, indicating a positive additional flow. If $MAP > MAP_0$, volume is removed from the circulation, representing blood pooling in the veins and fluid excretion through RAAS.

Preferential streaming pattern of the DV flow

In the full-term fetus, ~25% of the oxygen-rich blood from the umbilical vein passes through the DV^{119–121} and preferentially streams into the LA through the FO.⁴⁵ This preferential streaming pattern was taken into account in the CircAdapt model by forcing the oxygen saturation of the FO flow to consist primarily of umbilical vein oxygen saturation mixed with inferior vena cava (IVC) oxygen saturation. In case of positive FO flow (i.e., from RA to LA), the following equation holds:

$$SO_{2,FO} = \begin{cases} \frac{q_{FO}SO_{2,DV}}{q_{FO}} & \text{if } q_{FO} \leq q_{DV} \\ \frac{q_{FO}SO_{2,DV} + (q_{FO} - q_{DV})SO_{2,IVC}}{q_{FO}} & \text{else} \end{cases} \quad (A2)$$

with $SO_{2,FO}$ the oxygen saturation of the flow across the FO with a flow rate q_{FO} , $SO_{2,DV}$ the oxygen saturation of the flow across the DV with a flow rate q_{DV} , and $SO_{2,IVC}$ the oxygen saturation of the flow in the IVC with a flow rate q_{IVC} . According to Eq. (A2), the FO flow consists solely of blood originating from the DV if $q_{DV} > q_{FO}$. Otherwise, if $q_{DV} < q_{FO}$, the FO flow consist of blood originating from the DV with the remainder derived from the IVC.

REFERENCES

- Kiserud, T., Eik-Nes, S. H., Blaas, H.-G. & Hellevik, L. R. Foramen ovale: an ultrasonographic study of its relation to the inferior vena cava, ductus venosus and hepatic veins. *Ultrasound Obstet. Gynecol.* **2**, 389–396 (1992).
- Reed, K., Appleton, C., Sahn, C. & Anderson, C. Human fetal tricuspid and mitral deceleration time: changes with normal pregnancy and intrauterine growth retardation. *Am. J. Obstet. Gynecol.* **161**, 1532–1535 (1989).
- Baschat, A. A. The fetal circulation and essential organs - a new twist to an old tale. *Ultrasound Obstet. Gynecol.* **27**, 349–354 (2006).
- Rudolph, A. M. *Congenital Diseases of the Heart* 3rd edn (Wiley-Blackwell, 2009).
- Teitel, D. F., Iwamoto, H. S. & Rudolph, A. M. Changes in the pulmonary circulation during birth-related events. *Pediatr. Res.* **27**, 372–378 (1990).
- Crossley, K. J. et al. Dynamic changes in the direction of blood flow through the ductus arteriosus at birth. *J. Physiol.* **587**, 4695–4704 (2009).
- Sá-Couto, C. D., Andriessen, P., Van Meurs, W. L., Ayres-De-Campos, D. & Sá-Couto, P. M. A model for educational simulation of hemodynamic transitions at birth. *Pediatr. Res.* **67**, 158–165 (2010).
- Yigit, M. B., Kowalski, W. J., Hutchon, D. J. R. & Pekkan, K. Transition from fetal to neonatal circulation: modeling the effect of umbilical cord clamping. *J. Biomech.* **48**, 1662–1670 (2015).
- Huikeshoven, F., Coleman, T. G. & Jongsma, H. W. Mathematical model of the fetal cardiovascular system: the uncontrolled case. *Am. J. Physiol.* **8**, R317–R325 (1980).
- Huikeshoven, F. J., Hope, I. D. & Power, G. G. Mathematical model of fetal circulation and oxygen delivery. *Am. J. Physiol.* **18**, 192–202 (1985).
- Guettouche, A. et al. Mathematical modeling of the human fetal arterial blood circulation. *Int. J. Biomed. Comput.* **31**, 127–139 (1992).
- Guettouche, A., Papapanayotou, C., Cherruault, Y., Azancot-Benisty, A. & Challier, J. C. Optimization and resolution algorithm of the human fetal blood circulation model. *Math. Comput. Model.* **18**, 1–8 (1993).
- Thompson, R. & Trudinger, B. Doppler waveform pulsatility index and resistance, pressure and flow in the umbilical placental circulation: an investigation using a mathematical model. *Ultrasound Med. Biol.* **16**, 449–458 (1990).
- Costa, A., Costantino, M. & Fumero, R. Oxygen exchange mechanisms in the human placenta: mathematical modelling and simulation. *J. Biomed. Eng.* **14**, 385–389 (1992).
- Tulzer, G. et al. Diastolic function of the fetal heart during second and third trimester: a prospective longitudinal Doppler-echocardiographic study. *Eur. J. Pediatr.* **153**, 151–154 (1994).
- Pennati, G., Bellotti, M. & Fumero, R. Mathematical modelling of the human fetal cardiovascular system based on Doppler ultrasound data. *Med. Eng. Phys.* **19**, 327–335 (1997).
- Arts, T., Delhaas, T., Bovendeerd, P., Verbeek, X. & Prinzen, F. W. Adaptation to mechanical load determines shape and properties of heart and circulation: the CircAdapt model. *Am. J. Physiol.* **288**, 1943–1954 (2005).

- Lumens, J., Delhaas, T., Kirn, B. & Arts, T. Three-wall segment (TriSeg) model describing mechanics and hemodynamics of ventricular interaction. *Ann. Biomed. Eng.* **37**, 2234–2255 (2009).
- Koeken, Y., Kuijpers, N. H. L., Lumens, J., Arts, T. & Delhaas, T. Atrial septostomy benefits severe pulmonary hypertension patients by increase of left ventricular preload reserve. *Am. J. Physiol. Circ. Physiol.* **302**, H2654–H2662 (2012).
- Lumens, J. & Delhaas, T. Cardiovascular modeling in pulmonary arterial hypertension: Focus on mechanisms and treatment of right heart failure using the CircAdapt model. *Am. J. Cardiol.* **110**, S39–S48 (2012).
- Lumens, J. et al. Relative impact of right ventricular electromechanical dyssynchrony versus pulmonary regurgitation on right ventricular dysfunction and exercise intolerance in patients after repair of tetralogy of fallot. *J. Am. Heart Assoc.* **8**, e010903 (2019).
- Walmsley, J., Squara, P., Wolfhard, U., Cornelussen, R. & Lumens, J. Impact of abrupt versus gradual correction of mitral and tricuspid regurgitation: a modelling study. *EuroIntervention* **15**, 902–911 (2019).
- Heusinkveld, M. H. G. et al. Large vessels as a tree of transmission lines incorporated in the CircAdapt whole-heart model: a computational tool to examine vessel-vessel interaction. *PLoS Comput. Biol.* **15**, e1007173 (2019).
- Kuijpers, N. H. L. et al. CircAdapt: a user-friendly learning environment for (patho) physiology of heart and circulation. *Comput. Cardiol.* **39**, 969–972 (2012).
- Koeken, Y., Arts, T. & Delhaas, T. Simulation of the Fontan circulation during rest and exercise. In *Proc. Annual International Conference of IEEE Engineering in Medicine and Biology Society*. 6673–6676 (IEEE, 2012).
- Delhaas, T., Koeken, Y., Latus, H., Apitz, C. & Schranz, D. Potts Shunt to be preferred above atrial septostomy in pediatric pulmonary arterial hypertension patients: a modeling study. *Front. Physiol.* **9**, 1–7 (2018).
- Villar, J. et al. International standards for newborn weight, length, and head circumference by gestational age and sex: the Newborn Cross-Sectional Study of the INTERGROWTH-21st Project. *Lancet* **384**, 857–868 (2014).
- Arts, T., Bovendeerd, P. H., Prinzen, F. W. & Reneman, R. S. Relation between left ventricular cavity pressure and volume and systolic fiber stress and strain in the wall. *Biophys. J.* **59**, 93–102 (1991).
- Friedman, W. F. The intrinsic physiologic properties of the developing heart. *Prog. Cardiovasc. Dis.* **XV**, 87–111 (1972).
- St John Sutton, M., Gill, T., Plappert, T., Saltzman, D. H. & Doubilet, P. Assessment of right and left ventricular function in terms of force development with gestational age in the normal human fetus. *Br. Heart J.* **66**, 285–289 (1991).
- Hecher, K., Campbell, S., Snijders, R. & Nicolaides, K. Reference ranges for fetal venous atrioventricular blood flow parameters. *Ultrasound Obstet. Gynecol.* **4**, 381–390 (1994).
- Carceller-Blanchard, A. M. & Fouron, J. C. Determinants of the Doppler flow velocity profile through the mitral valve of the human fetus. *Br. Heart J.* **70**, 457–460 (1993).
- Reed, K. L. et al. Cardiac Doppler flow velocities in human fetuses. *Circulation* **73**, 41–46 (1986).
- Messing, B. et al. Fetal heart ventricular mass obtained by STIC acquisition combined with inversion mode and VOCAL. *Ultrasound Obstet. Gynecol.* **38**, 191–197 (2011).
- Hamill, N. et al. Fetal cardiac ventricular volume, cardiac output, and ejection fraction determined with 4-dimensional ultrasound using spatiotemporal image correlation and virtual organ computer-aided analysis. *Am. J. Obstet. Gynecol.* **205**, 76.e1–76.e10 (2011).
- Messing, B. et al. Fetal cardiac ventricle volumetry in the second half of gestation assessed by 4D ultrasound using STIC combined with inversion mode. *Ultrasound Obstet. Gynecol.* **30**, 142–151 (2007).
- Esh-Broder, E., Ushakov, F. B., Imbar, T. & Yagel, S. Application of free-hand three-dimensional echocardiography in the evaluation of fetal cardiac ejection fraction: a preliminary study. *Ultrasound Obstet. Gynecol.* **23**, 546–551 (2004).
- Palau-Caballero, G., Walmsley, J., Gorcsan, J., Lumens, J. & Delhaas, T. Abnormal ventricular and aortic wall properties can cause inconsistencies in grading aortic regurgitation severity: a computer simulation study. *J. Am. Soc. Echocardiogr.* **29**, 1122–1130.e4 (2016).
- Kiserud, T. & Rasmussen, S. Ultrasound assessment of the fetal foramen ovale. *Ultrasound Obstet. Gynecol.* **17**, 119–124 (2001).
- Feit, L. R., Copel, J. A. & Kleinman, C. S. Foramen ovale size in the normal and abnormal human fetal heart: an indicator of transatrial flow physiology. *Ultrasound Obstet. Gynecol.* **1**, 313–319 (1991).
- Arts, T., Reesink, K., Kroon, W. & Delhaas, T. Simulation of adaptation of blood vessel geometry to flow and pressure: implications for arterio-venous impedance. *Mech. Res Commun.* **42**, 15–21 (2012).
- Reymond, P., Merenda, F., Perren, F., Rufenacht, D. & Stergiopoulos, N. Validation of a one-dimensional model of the systemic arterial tree. *Am. J. Physiol.* **297**, H208–H222 (2009).

43. Müller, L. O. & Toro, E. F. A global multiscale mathematical model for the human circulation with emphasis on the venous system. *Int. J. Numer. Method Biomed. Eng.* **30**, 681–725 (2014).
44. Stringer, M. D. Anatomy of the infant and child. In *Pediatr. Surg.* 1–19 (Springer, 2017).
45. Kiserud, T. Physiology of the fetal circulation. *Semin. Fetal Neonatal Med.* **10**, 493–503 (2005).
46. Acharya, G. & Sitras, V. Oxygen uptake of the human fetus at term. *Acta Obstet. Gynecol. Scand.* **88**, 104–109 (2009).
47. Nodwell, A., Carmichael, L., Ross, M. & Richardson, B. Placental compared with umbilical cord blood to assess fetal blood gas and acid-base status. *Obstet. Gynecol.* **105**, 129–138 (2005).
48. Arikani, G. M. et al. Cord blood oxygen saturation in vigorous infants at birth: What is normal? *Br. J. Obstet. Gynaecol.* **107**, 987–994 (2000).
49. Richardson, B. S. et al. Fetal oxygen saturation and fractional extraction at birth and the relationship to measures of acidosis. *Am. J. Obstet. Gynecol.* **178**, 572–579 (1998).
50. Lackman, F., Capewell, V., Gagnon, R. & Richardson, B. Fetal umbilical cord oxygen values and birth to placental weight ratio in relation to size at birth. *Am. J. Obstet. Gynecol.* **185**, 674–682 (2001).
51. Hall, J. *Guyton and Hall: textbook of medical physiology* 1st edn (Elsevier, 2016).
52. Altuncu, E., Özek, E., Bilgen, H., Topuzoglu, A. & Kavuncuoğlu, S. Percentiles of oxygen saturations in healthy term newborns in the first minutes of life. *Eur. J. Pediatr.* **167**, 687–688 (2008).
53. Rabi, Y., Yee, W., Chen, S. Y. & Singhal, N. Oxygen saturation trends immediately after birth. *J. Pediatr.* **148**, 590–594 (2006).
54. Mariani, G. et al. Pre-ductal and post-ductal O₂ saturation in healthy term neonates after birth. *J. Pediatr.* **150**, 418–421 (2007).
55. Kamlin, C. O. F., O'Donnell, C. P. F., Davis, P. G. & Morley, C. J. Oxygen saturation in healthy infants immediately after birth. *J. Pediatr.* **148**, 585–589 (2006).
56. Toth, B., Becker, A. & Seelbach-Göbel, B. Oxygen saturation in healthy newborn infants immediately after birth measured by pulse oximetry. *Arch. Gynecol. Obstet.* **266**, 105–107 (2002).
57. Dimich, I. et al. Evaluation of oxygen saturation monitoring by pulse oximetry in neonates in the delivery system. *Can. J. Anesth.* **38**, 985–988 (1991).
58. Deckardt, R., Schneider, K. T. M. & Graeff, H. Monitoring arterial oxygen saturation in the neonate. *J. Perinat. Med.* **15**, 357–364 (1987).
59. House, J. T., Schultetus, R. R. & Gravenstein, N. Continuous neonatal evaluation in the delivery room by pulse oximetry. *J. Clin. Monit. Comput.* **3**, 96–100 (1987).
60. Harris, A. P., Sendak, M. J. & Donham, R. T. Changes in arterial oxygen saturation immediately after birth in the human neonate. *J. Pediatr.* **109**, 117–119 (1986).
61. Reddy, V. K., Holzman, R. & Wedgwood, J. F. Pulse oximetry saturations in the first 6 h of life in normal term infants. *Clin. Pediatr.* **38**, 87–92 (1999).
62. Hooper, S. B. & Harding, R. Role of aeration in the physiological adaptation of the lung to air-breathing at birth. *Curr. Respir. Med. Rev.* **1**, 185–195 (2005).
63. Friedman, A. & Fahey, J. The transition from fetal to neonatal circulation: normal responses and implications for infants with heart disease. *Semin. Perinatol.* **17**, 106–121 (1993).
64. Ghanayem, N. S. & Gordon, J. B. Modulation of pulmonary vasomotor tone in the fetus and neonate. *Respir. Res.* **2**, 139–144 (2001).
65. Dawes, G. S., Mott, J. C., Widdicombe, J. G. & Wyatt, D. G. Changes in the lungs of the new-born lamb. *J. Physiol.* **121**, 141–162 (1953).
66. Emmanouilides, G. C., Moss, A. J., Duffie, E. R. & Adams, F. H. Pulmonary arterial pressure changes in human newborn infants from birth to 3 days of age. *J. Pediatr.* **65**, 327–333 (1964).
67. Moss, A. & Emmanouilides, G., Pediatrics FA-, 1964 U. Response of ductus arteriosus and pulmonary and systemic arterial pressure to changes in oxygen environment in newborn infants. *Pediatrics* **33**, 937–944 (1964).
68. Anderson, D. F., Bissonnette, J. M., Faber, J. J. & Thornburg, K. L. Central shunt flows and pressures in the mature fetal lamb. *Am. J. Physiol.* **241**, H60–H66 (1981).
69. van Vonderen, J. et al. Noninvasive measurements of hemodynamic transition at birth. *Pediatr. Res.* **75**, 1–5 (2014).
70. Noori, S. et al. Transitional changes in cardiac and cerebral hemodynamics in term neonates at birth. *J. Pediatr.* **160**, 943–948 (2012).
71. Agata, Y. et al. Changes in left ventricular output from fetal to early neonatal life. *J. Pediatr.* **119**, 441–445 (1991).
72. Kishkurno, S. et al. Postnatal changes in left ventricular volume and contractility in healthy term infants. *Pediatr. Cardiol.* **18**, 91–95 (1997).
73. Shiota, T., Herada, K. & Takada, G. Left ventricular systolic and diastolic function during early neonatal period using transthoracic echocardiography. *J. Exp. Med.* **197**, 151–158 (2002).
74. Hiraishi, S. et al. Two-dimensional Doppler echocardiographic assessment of closure of the ductus arteriosus in normal newborn infants. *J. Pediatr.* **111**, 755–760 (1987).
75. Kajino, H. et al. Factors that increase the contractile tone of the ductus arteriosus also regulate its anatomic remodeling. *Am. J. Physiol.* **281**, R291–R301 (2001).
76. Clyman, R. I. Mechanisms regulating the ductus arteriosus. *Biol. Neonate* **89**, 330–335 (2006).
77. Hermes-DeSantis, E. & Clyman, R. I. Patent ductus arteriosus: pathophysiology and management. *J. Perinatol.* **26**, S1–S14 (2006).
78. Rasanen, J., Wood, D. C., Weiner, S., Ludomirski, A. & Huhta, J. C. Role of the pulmonary circulation in the distribution of human fetal cardiac output during the second half of pregnancy. *Circulation* **94**, 1068–1073 (1996).
79. Walther, F. J., Benders, M. J. & Leighton, J. O. Early changes in the neonatal circulatory transition. *J. Pediatr.* **123**, 625–632 (1993).
80. St John Sutton, M., Groves, A., MacNeill, A., Sharland, G. & Allan, L. Assessment of changes in blood flow through the lungs and foramen ovale in the normal human fetus with gestational age: a prospective Doppler echocardiographic study. *Br. Heart J.* **71**, 232–237 (1994).
81. Tan, J., Silverman, N. H., Hoffman, J. I. E., Villegas, M. & Schmidt, K. G. Cardiac dimensions determined by cross-sectional echocardiography in the normal human fetus from 18 weeks to term. *Am. J. Cardiol.* **70**, 1459–1467 (1992).
82. Coskun, S. et al. Non-invasive evaluation of the adaptations of cardiac function in the neonatal period: a comparison of healthy infants delivered by vaginal route and caesarean section. *Acta Med. Okayama.* **55**, 213–218 (2001).
83. Versmold, H. T., Kitterman, J. A., Phibbs, R. H., Gregory, G. A. & Tooley, W. H. Aortic blood pressure during the first 12 hours of life in infants with birth weight 610 to 4,220 grams. *Pediatrics* **67**, 607–613 (1981).
84. Struijk, P. C. et al. Blood pressure estimation in the human fetal descending aorta. *Ultrasound Obstet Gynecol.* **32**, 673–681 (2008).
85. Seed, M. et al. Feasibility of quantification of the distribution of blood flow in the normal human fetal circulation using CMR: a cross-sectional study. *J. Cardiovasc. Magn. Reson.* **14**, 1–11 (2012).
86. Kiserud, T., Ebbing, C., Kessler, J. & Rasmussen, S. Fetal cardiac output, distribution to the placenta and impact of placental compromise. *Ultrasound Obstet. Gynecol.* **28**, 126–136 (2006).
87. Mielke, G. & Benda, N. Cardiac output and central distribution of blood flow in the human fetus. *Circulation* **103**, 1662–1668 (2001).
88. Meyer-Wittkopf, M., Cole, A., Cooper, S. G., Schmidt, S. & Sholler, G. F. Three-dimensional quantitative echocardiographic assessment of ventricular volume in healthy human fetuses and in fetuses with congenital heart disease. *J. Ultrasound Med.* **20**, 317–327 (2001).
89. de Smedt, M. C. H., Visser, G. H. A. & Meijboom, E. J. Fetal cardiac output estimated by Doppler echocardiography during mid- and late gestation. *Am. J. Cardiol.* **60**, 338–342 (1987).
90. Kenny, J. F. et al. Changes in intracardiac blood flow velocities and right and left ventricular stroke volumes with gestational age in the normal human fetus: a prospective Doppler echocardiographic study. *Circulation* **74**, 1208–1216 (1986).
91. Chaoui, R., Heling, K., Taddei, F. & Bollmann, R. Doppler-echokardiographische Analyse des Blutflusses über den fetalen Aorten- und Pulmonalklappen in der zweiten Hälfte der Schwangerschaft. *Geburtshilfe Frauenheilkd.* **55**, 2017–2217 (1995).
92. Oberhoffer, R., Högel, J. & Lang, D. Normal characteristics of cardiac dimensions and function in the fetus. *Eur. J. Ultrasound* **2**, 93–106 (1995).
93. Allan, L. D., Chita, K., Al-Ghazali, W., Crawford, D. C. & Tynan, M. Doppler echocardiographic evaluation of the normal human fetal heart. *Br. Heart J.* **57**, 528–561 (1987).
94. Shah, S. & Maheshwari, S. Fetal echocardiography. *J. Neonatology* **22**, 154–159 (2018).
95. Schmidt, K. G., Silverman, N. H. & Hoffman, J. I. E. Determination of ventricular volumes in human fetal hearts by two-dimensional echocardiography. *Am. J. Cardiol.* **76**, 1313–1316 (1995).
96. Pineda, F. L. et al. Contribution of Doppler atrioventricular flow waves to ventricular filling in the human fetus. *Pediatr. Cardiol.* **21**, 422–428 (2000).
97. Johnson, P., Maxwell, D. J., Tynan, M. J. & Allan, L. D. Intracardiac pressures in the human fetus. *Heart* **84**, 59–63 (2000).
98. Reller, M., Morton, M., Reid, D. & Thornburg, K. L. Fetal lamb ventricles respond differently to filling and arterial pressures and to in utero ventilation. *Pediatr. Res.* **22**, 621–626 (1987).
99. Morin, F. C. & Egan, E. A. Pulmonary hemodynamics in fetal lambs during development at normal and increased oxygen tension. *J. Appl. Physiol.* **73**, 213–218 (1992).
100. Teitel, D. F., Iwamoto, H. S. & Rudolph, A. M. Effects of birth-related events on central blood flow patterns. *Pediatr. Res.* **22**, 557–566 (1987).
101. Anderson, D. F., Bissonnette, J. M., Faber, J. J. & Thornburg, K. L. Central shunt flows and pressures in the mature fetal lamb. *Am. J. Physiol. Circ. Physiol.* **241**, H60–H66 (1981).
102. Mielke, G., Steil, E., Kendziorra, H. & Goelz, R. Ductus arteriosus-dependent pulmonary circulation secondary to cardiac malformations in fetal life. *Ultrasound Obstet Gynecol.* **9**, 25–29 (1997).
103. Mielke, G., Steil, E., Breuer, J. & Goelz, R. Circulatory changes following intrauterine closure of the ductus arteriosus in the human fetus and newborn. *Prenat. Diagn.* **18**, 139–145 (1998).

104. Grant, D. A., Hollander, E., Skuza, E. M. & Fauchère, J. C. Interactions between the right ventricle and pulmonary vasculature in the fetus. *J. Appl. Physiol.* **87**, 1637–1643 (1999).
105. Hooper, S. B. et al. Cardiovascular transition at birth: a physiological sequence. *Pediatr. Res.* **77**, 608–614 (2015).
106. Bhatt, S. et al. Delaying cord clamping until ventilation onset improves cardiovascular function at birth in preterm lambs. *J. Physiol.* **591**, 2113–2126 (2013).
107. Wilson, N., Reed, K., Allen, H., Marx, G. & Goldberg, S. Doppler echocardiographic observations of pulmonary and transvalvular velocity changes after birth and during the early neonatal period. *Am. Heart J.* **113**, 750–758 (1987).
108. Yao, A., Hirvensalo, M. & Lind, J. Placental transfusion-rate and uterine contraction. *Lancet* **291**, 380–383 (1968).
109. Moinian, M., Meyer, W. W. & Lind, J. Diameters of umbilical cord vessels and the weight of the cord in relation to clamping time. *Am. J. Obstet. Gynecol.* **105**, 604–611 (1969).
110. Rao, R. & Ramji, S. Pulse oximetry in asphyxiated newborns in the delivery room. *Indian Pediatr.* **38**, 762–765 (2001).
111. Agata, Y. et al. Regional blood flow distribution and left ventricular output during early neonatal life: a quantitative ultrasonographic assessment. *Pediatr. Res.* **36**, 805–810 (1994).
112. Harada, K., Shiota, T., Takahashi, Y., Tamura, M. & Takada, G. Changes in the volume and performance of the left ventricle in the early neonatal period. *Early Hum. Dev.* **39**, 201–209 (1994).
113. Winberg, P., Jansson, M., Marions, L. & Lundell, W. Left ventricular output during postnatal circulatory adaptation in healthy infants born at full term. *Arch. Dis. Child* **64**, 1374–1378 (1989).
114. Roos, A. Poiseuille's law and its limitations in vascular systems. *Respiration* **19**, 224–238 (1962).
115. Kondo, M. et al. Pressure-flow relationship and longitudinal distribution of pulmonary vascular resistance in heartworm-infected dogs. *J. Vet. Med. Sci.* **65**, 965–970 (2003).
116. Rudolph, A. M. & Auld, P. A. Physical factors affecting normal and serotonin-constricted pulmonary vessels. *Am. J. Physiol.* **198**, 864–872 (1960).
117. Permutt, S. Recruitment versus distensibility in the pulmonary vascular bed. In *Pulm. Circ. Interstitial Sp.* 375–390 (eds Fishman, A. P. & Hecht, H. H.) (1969).
118. Culver, B. H. & Butler, J. Mechanical influences on the pulmonary microcirculation. *Annu. Rev. Physiol.* **42**, 187–198 (1980).
119. Haugen, G., Kiserud, T., Godfrey, K., Crozier, S. & Hanson, M. Portal and umbilical venous blood supply to the liver in the human fetus near term. *Ultrasound Obstet. Gynecol.* **24**, 599–605 (2004).
120. Bellotti, M., Pennati, G., De Gasperi, C., Battaglia, F. C. & Ferrazzi, E. Role of ductus venosus in distribution of umbilical blood flow in human fetuses during second half of pregnancy. *Am. J. Physiol.* **279**, 1256–1263 (2000).
121. Kiserud, T., Rasmussen, S. & Skulstad, S. Blood flow and the degree of shunting through the ductus venosus in the human fetus. *Am. J. Obstet. Gynecol.* **182**, 147–153 (2000).